Fission fragment yield distribution in the heavy-mass region from the ^{239}Pu (n_{th}, f) reaction

Y. K. Gupta and D. C. Biswas
Nuclear Physics Division, Bhabha Atomic Research Centre, Mumbai 400085, India

O. Serot, D. Bernard, and O. Litaize
CEA, DEN, DER, SPRC, Physics Studies Laboratory, Cadarache, F-13108 Saint Paul Lez Durance, France

S. Julien-Laferrière, A. Chebboubi, G. Kessedjian, and C. Sage
LPSC, Université Grenoble-Alpes, F-38000 Grenoble, France

A. Blanc, H. Faust, and U. Köster
Institut Laue Langevin, F-38042 Grenoble, France

A. Ebran
CEA, DAM-Bruyères-Le-Châtel, F-91290 Arpajon, France

L. Mathieu
CEN Bordeaux Gradignan, F-33175 Gradignan, France

A. Letourneau, T. Materna, and S. Panebianco
CEA, DRF-Saclay, F-91191 Gif-sur-Yvette, France

(Received 13 February 2017; revised manuscript received 17 April 2017; published 13 July 2017)

The fission fragment yield distribution has been measured in the ^{239}Pu(n_{th}, f) reaction in the mass region of $A = 126$ to 150 using the Lohengrin recoil-mass spectrometer. Three independent experimental campaigns were performed, allowing a significant reduction of the uncertainties compared to evaluated nuclear data libraries. The long-standing discrepancy of around 10% for the relative yield of $A = 134$ reported in JEF-2.2 and JEFF-3.1.1 data libraries is finally solved. Moreover, the measured mass distribution in thermal neutron-induced fission does not show any significant dip around the shell closure ($A = 136$) as seen in heavy-ion fission data of ^{208}Pb(^{18}O, f) and ^{238}U(^{18}O, f) reactions. Lastly, comparisons between our experimental data and the predictions from Monte Carlo codes (GEF and FIFRELIN) are presented and discussed.

DOI: 10.1103/PhysRevC.96.014608

I. INTRODUCTION

Dynamical evolution during nuclear fission involves intrinsic excitations and a large-scale collective rearrangement of the nuclear many-body system. Fission observables such as mass yield, charge yield, fission-fragment kinetic energy distribution, etc., provide important clues to understand the nuclear fission process. Numerous theoretical models [1–5] have been developed with limited success to obtain a consistent picture of the fission observables. Fission fragment (FF) mass distribution is one of the most important characteristics of the nuclear fission process. Mass split during the descent from saddle to scission points, in particular for the cold nuclei, is governed by the superposition of nuclear shell effects of the nascent fragments with the liquid drop potential energy of the fissioning nucleus [2]. Despite sustained efforts both theoretically as well as experimentally during the past several decades to understand the complex fission process, it is still a topic of continued research interest.

In addition to the understanding of the fission dynamics, precise information about the fission mass yields from neutron-induced fission plays a key role in designing the new nuclear technologies. A vast amount of experimental data has been accumulated over the years from thermal neutron-induced fission of actinide nuclei and is incorporated into evaluated nuclear data libraries such as JEF-2.2 [6], JEFF-3.1.1 [7], ENDF/B-VII.0 [8], and JENDL-4.0 [9]. Nevertheless, further efforts are needed to reduce fission yield uncertainties as well as to understand the differences observed between these evaluated nuclear data libraries.

In the case of ^{239}Pu(n_{th}, f) reaction, anomalies in the mass distribution around $A = 134$ have been observed; e.g., revised data library JEFF-3.1.1 [7] shows a dip of about 10% in comparison to the JEF-2.2 [6] for $A = 134$. The independent mass yield for $A = 134$ roughly corresponds to the ^{134}Xe cumulated fission yield. Since xenon is released in irradiated Mixed Oxide (MOX) fuel, its accurate production information is very important for the nuclear energy reactors.

Moreover, in heavy-ion-induced fusion-fission reactions it has been reported that the mass distributions show fine structure dips at $A = 124$ and 136 in ^{208}Pb(^{18}O, f) [10,11] and ^{238}U(^{18}O, f) [12] reactions. These experiments are performed at large excitation energies (∼35 to 55 MeV) of the fissioning nuclei and the mass yield is determined from fission-fragment γ-ray spectroscopy. The observed dips in the mass-yield distribution have been interpreted in terms of shape inhibition

TABLE I. Characteristics of the samples used for the three experiments.

Campaign	Measured masses	Target thickness (μg/cm^2)	Ni foil (μm)	Target size (cm^2)
Experiment 1 (2009) [15]	126–150	107	0.25	0.8×7
Experiment 2 (2011) [16]	132–145	300	0.25	0.8×7
Experiment 3 (2014) [17]	90,98,108, 130–138, and 140–143	103	0.25	1×7

around the closed shell ($Z = 50$ and $N = 82$) fragment nuclei at the scission point [12]. Shell effects are more prominent at lower excitation energies; therefore, it would be very interesting to investigate the fine structures in mass distributions of the cold fissioning nuclei such as from thermal neutron-induced fission.

Since 2008, in the frame of a large collaboration, we started measurements of fission yields for various fissioning nuclei, mainly in the heavy mass region, using the Lohengrin recoil-mass spectrometer located at the Institut Laue-Langevin (ILL) in Grenoble (France) [13]. In the present paper, we report the results obtained for mass distribution in the range of $A = 126$–150 from ^{239}Pu($n_{\rm th}$, f) reaction, measured in three independent experiment campaigns.

II. EXPERIMENTAL TECHNIQUES

The Lohengrin recoil-mass spectrometer is an instrument for studying nuclear physics that uses low-energy fission reactions for fission fragments production [14]. The fission yield data were taken in three different experiments, carried out in 2009 [15], 2011 [16], and 2014 [17], covering different mass ranges. Characteristic parameters of these three experiments are shown in Table I. The targets used in these experiments were highly enriched ^{239}Pu (99.5%) deposited as oxide on a titanium backing of rectangular shape (70 × 10 mm^2) with thickness of 0.5 mm. The ^{239}Pu mass of the target was in the range of 103 to 300 μg/cm^2, as shown in Table I. It was covered by a diaphragm, holding a Ni foil to reduce the self-sputtering [18]. The thicknesses of the Ni foil and opening areas (or effective sizes of the target) used in each experiment are shown in Table I. Typical mass resolution was of the order of $A/\Delta A \simeq 400$. The sample was placed close to the core of ILL's high-flux reactor in a thermal-neutron flux of 5×10^{14} n/cm^2 s. Owing to the high enrichment and to the high thermal fission cross section of ^{239}Pu, contributions from other isotopes of plutonium were negligible.

Fission products emerging from the target are produced in a wide range of ionic charge states, q, ranging from about 15 to 30 and kinetic energies, E_k, from about 30 to 110 MeV, depending on their masses. The selection of the fission products is performed by a combination of a magnetic and an electric sector fields, whose deflections are perpendicular to each other. At the exit slit of this parabola spectrometer, the combined action of the two fields separates different ions according to their A/q and E_k/q ratios. Since several nuclei can have the same A/q and E_k/q ratios, a ΔE-E gas-ionization telescope is employed at the exit slit of the spectrometer, where different mass fragments are separated in the ΔE vs E plot as shown in Fig. 1 for a typical setting of the spectrometer, having $A/q = 5.0$ and $E_k/q = 5.0$.

The flight path for the fission products is 23 m long, which results in a time of flight of about 2 μs, so that the fission products reach the gas-ionization telescope before undergoing the β decay and before emission of delayed neutrons. Details on the Lohengrin mass spectrometer can be found in Refs. [19,20].

III. DATA ANALYSIS AND RESULTS

The yield, $Y(A,q,E_k)$, corresponding to a particular mass number A, ionic charge q, and kinetic energy E_k, is extracted from the two-dimensional plot of ΔE vs E. In principle, mass yield $Y(A)$ should be determined by integrating over all kinetic energies and all ionic charges, which is by far much too time-consuming. We have employed two approaches to reduce the experimental time. The first one was applied for experiments 1 and 2, while the second approach was applied for experiment 3.

A. Procedure used for experiments 1 and 2

Assuming kinetic energy distribution to be independent of ionic charge distribution, we have used the following experimental procedure for the first two experiments. First, the ionic charge is scanned at an optimum kinetic energy $E_k^{\rm opt}$, from where the fraction of optimum charge $q_m^{\rm frac}$ of E scan is

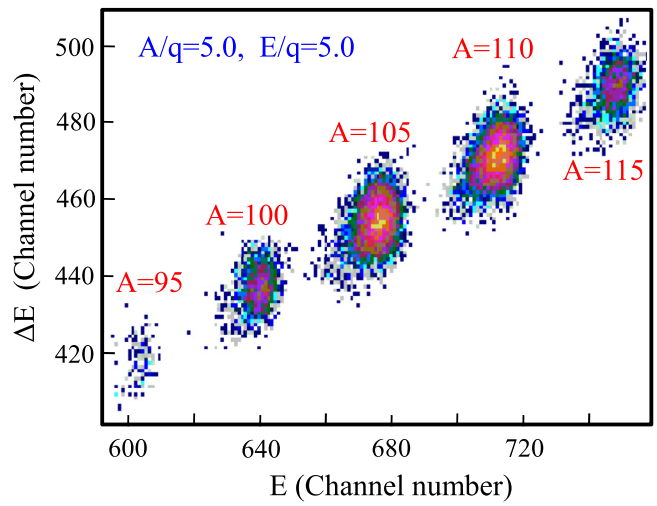

FIG. 1. A two-dimensional plot of ΔE vs E for a typical setting of the spectrometer $A/q = 5.0$ and $E_k/q = 5.0$.

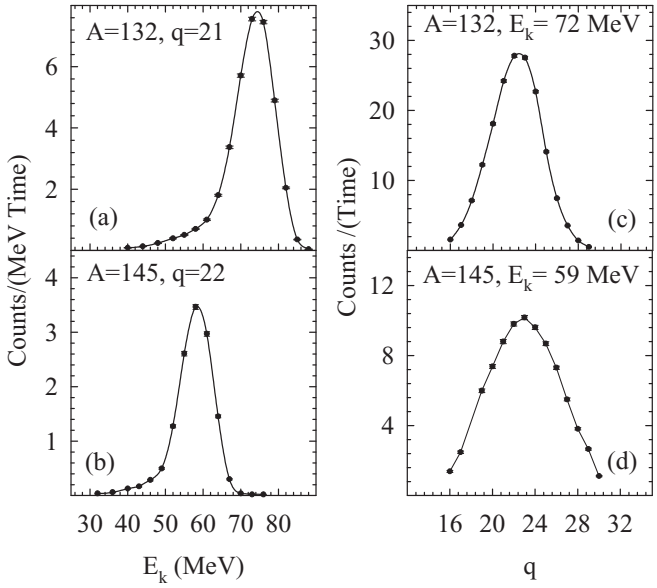

FIG. 2. Typical distributions of kinetic energies [panels (a) and (b)] and ionic charges [panels (c) and (d)] for the two masses $A = 132$ and 145 (from experiment 2). In each panel, line is shown to guide the eye.

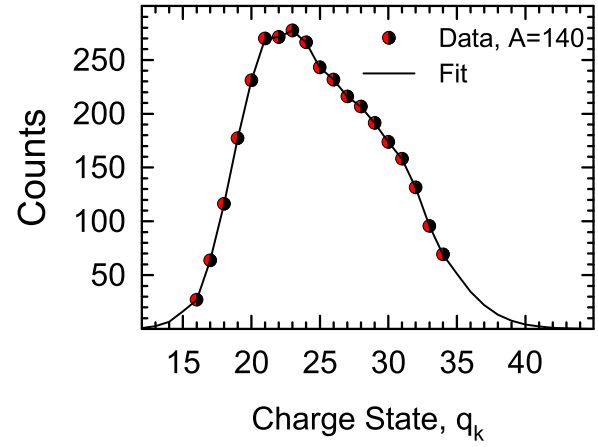

FIG. 3. Ionic charge distribution for $A = 140$ measured at kinetic energy of 62 MeV, an example of nanosecond isomer affecting the charge distribution (see text). The solid line represents the two peak Gaussian fit.

determined:

$$q_m^{\mathrm{frac}}(A) = \frac{Y\left(A, q_m, E_k^{\mathrm{opt}}\right)}{\int Y\left(A, q, E_k^{\mathrm{opt}}\right) dq}. \quad (1)$$

Then, measuring the E_k distribution at the optimum $q(q_m)$ and knowing what fraction of the total intensity is contained for a given (q_m), the total yield is determined by dividing the integration of E_k distribution by the q_m fraction:

$$Y(A) = \frac{\int \left(Y(A, q_m, E_k)/E_k\right) dE_k}{q_m^{\mathrm{frac}}(A)}. \quad (2)$$

Typical kinetic energy distributions measured at $q_m = 21$ and 22 for $A = 132$ and 145 are shown in Figs. 2(a) and 2(b), respectively. Typical ionic charge distributions for the same masses at $E_k^{\mathrm{opt}} = 72$ and 59 MeV are shown in Figs. 2(c) and 2(d), respectively.

It has to be noted here that the yields from E_k and q distributions are obtained by making Gaussian fits of the data. In some cases, such as $A = 140$, 142, and 144, a tail of high ionic charge state is observed which cannot be explained by a purely atomic considerations. This effect has been identified earlier as due to the presence of nanosecond isomers which decay by highly converted transitions and cause a second Gaussian peak in the charge distribution shifted by about 3 to 4 units of charge states toward the higher values [21,22]. In these cases, the q distribution is needed to be fitted with a two-peak Gaussian. This effect of nanosecond isomers in q distributions is more prevalent in case of $A = 140$, as shown in Fig. 3. This is due to the fact that yields of $A = 140$ have significant contributions from ^{140}Cs [15,23], which has at least two nanosecond isomers on top of each other [24].

This procedure is faster since only one scan across kinetic energies and one scan across ionic charges are needed; as already mentioned, it resides on the assumption that E_k and q distributions are independent of each other, which is not always true. Therefore, this procedure may results in less accurate mass yield data.

B. Procedure used for the experiment 3

For this last measurement campaign, an independent method has been developed in order to try to reduce the uncertainties on our data. The Gaussian-like fits (as used in the first two experimental campaigns) have been replaced by pure statistical analysis, which generates a statistical weight associated to each mass yield [17]. This method requires an accurate knowledge of the kinetic energy and ionic charge distributions, and therefore the whole distributions have to be covered. For that, we have checked that the minimum point of the distribution be lower than 0.5% of the maximum point. Then statistical weights are attributed to the fission mass yields using the normalization of all the points to the JEFF evaluation. The second difference for this method is that the correlation between kinetic energy distributions and ionic charge distributions is deduced from the data and taken into account in the uncertainty analysis [25]. Typically from 2 up to 4 scans across ionic charge at different kinetic energy were performed. At the end, from 2 up to 4 mass measurements have been obtained and compared in order to deduce a mean value per mass with a reduced uncertainty. We have checked that no bias was introduced when using the double Gaussian distribution procedure (as for experiments 1 and 2) and the pure statistical one (as for this experiment 3). More details on this specific analysis will be presented in another article [26].

C. Burnup measurement

Because of the high thermal neutron flux at the position of the source and the very high (n, f) and (n, γ) cross sections (total ~1000 b) for ^{239}Pu, the source (target) strength reduces quite appreciably over time. In order to determine normalized mass yields, the change of the source strength over time (due

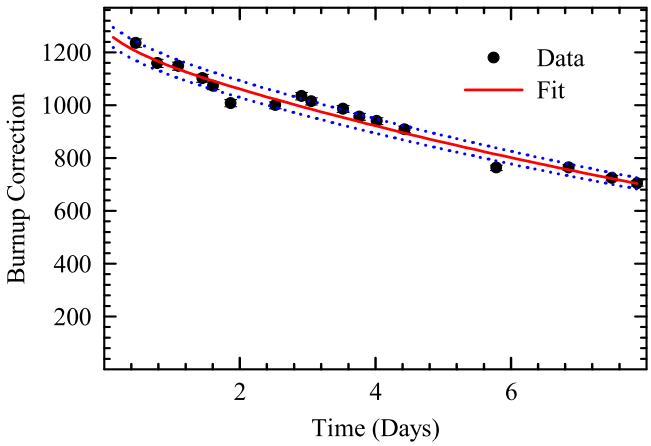

FIG. 4. An example of burn-up curve obtained from periodic yield measurement of $A = 136$. The solid line represent the fit obtained using Eq. (3). The dotted lines shows ±3% error, encompassing almost all measured values (see text).

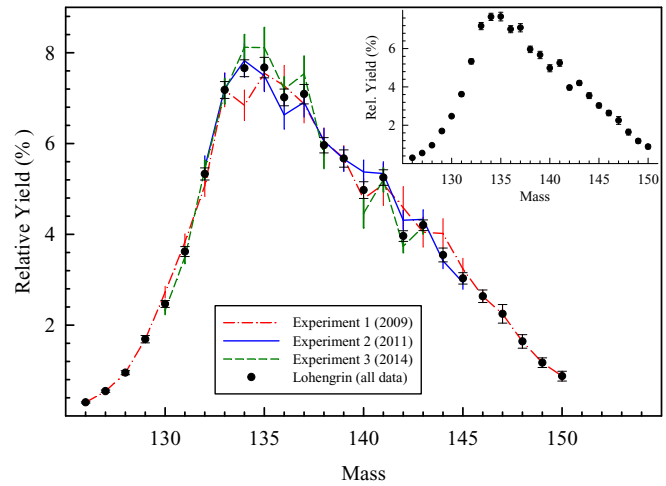

FIG. 5. Relative mass yields for thermal neutron-induced fission of ^{239}Pu from our three measurement campaigns. The final averaged experimental yields are also plotted (black circles) and are shown exclusively in the inset.

to nuclear burnup and self-sputtering) has to be taken into account [18]. For this purpose, measurements of the mass yield for $A = 136$ have been carried out periodically about every eight hours, resulting in the burn-up curve. A typical burn-up curve from experiment campaign 2 is shown in Fig. 4. The burn-up behavior is well described by the sum of two decreasing exponentials having two different decay constants, one fast (λ_f) and the other slow (λ_s) [15]:

$$BU(t) = I_s \exp(-\lambda_s t) + I_f \exp(-\lambda_f t), \quad (3)$$

where I_s, λ_s, I_f, and λ_f are the free parameters deduced from the fit. The yield for $A = 136$ is determined [using Eq. (2)] from the kinetic energy distribution in the range of 40 to 80 MeV at an optimum ionic charge state of $q_m = 21$, where the fraction of $q_m = 21$ is obtained from ionic charge distributions at an optimum kinetic energy $E_k^{\text{opt}} = 68$ MeV. It is seen that the peak values and the widths of kinetic energy distributions and ionic charge distributions for $A = 136$ remain nearly constant. For example, during the whole measurement period of around eight days for the experiment campaign 2, the fraction of $q_m = 21$ for $A = 136$ at $E_k^{\text{opt}} = 68$ MeV is observed to be fairly constant around 0.11. It is seen from Fig. 4 that ±3% error encompasses all the measured data for the yield of $A = 136$.

D. Results

In total, three independent sets of data on the ^{239}Pu(n_{th}, f) mass yields in the heavy fission fragment region have been measured at the Lohengrin mass spectrometer during the past decade: Bail *et al.* in 2009 [15] (experiment 1), Gupta *et al.* in 2011 [16] (experiment 2), and Chebboubi *et al.* in 2014 [17] (experiment 3).

Each dataset, normalized with a corresponding sum on JEFF-3.1.1, are reported in Table II with the total uncertainty (sum of the statistical and systematic uncertainties). The systematic errors were decomposed into three main components:

(1) the normalization, which has been estimated to be about 1%;

(2) the burn-up (strongly dependent of the sample behavior): The uncertainty is mainly governed by the uncertainty of the fit performed to reproduce the burn-up curve (see Fig. 4);

(3) the assumption that E_k and q distributions are independent of each other. The uncertainty related to this approximation was estimated to be lower than 2% (see Ref. [15]) and was applied only for experiments 1 and 2.

It is worth noting here that in experimental campaign 1, both isotopic yields $Y(A,Z)$ (using γ-ray spectroscopy technique) and mass yields $Y(A)$ (using an ionization chamber) were measured. The isotopic yields could be measured only to some masses as shown in the Table IV of the Ref. [15] due to the limitation of the γ-ray spectroscopy technique (half-life of the fission product, availability of the decay data, etc.). Data presented here in the Table II for experimental campaign 1 are solely the mass-yield data measured using the ionization chamber placed at the focal plane of the Lohengrin spectrometer.

From the three datasets, a mean value (weighted by their standard deviations) could be extracted in order to obtain the best experimental value of the partial mass yields for the ^{239}Pu(n_{th}, f) reaction. Figure 5 shows the comparison between the whole dataset as well as the averaged final data (black circles). The measured yields in our covered mass region ($A = [126–150]$) represents 96.69% of the total heavy-mass region. To first order, a good agreement is observed between all measurements, except for the mass $A = 134$ and $A = 142$, where a discrepancy higher than 18% between experiments is observed for both masses. Nevertheless, a χ^2 test has been performed (last column of Table II). According to the χ^2 tables, if the calculated χ^2 is higher than 7.88 (for a distribution with one degree of freedom) or 10.60 (for a distribution with two degrees of freedom), then the experimental data must be rejected. As shown in Table II, this is never the case. It means that within three standard deviations, data from the three

TABLE II. Mass yields (in %) with their total relative uncertainties for the three independent experimental campaigns related to ^{239}Pu(n_{th}, f) reaction. Final results obtained by averaging the three datasets weighted by the error bars are also given. The last column corresponds to the χ^2 values calculated when two or three sets of experimental data are available, showing that within three standard deviations (confidence level at 99.5%), data from the three experiments are consistent each other (see text).

Mass	Experiment 1	Experiment 2	Experiment 3	Average value	χ^2
126	0.298 ± 0.015			0.298 ± 0.015	
127	0.545 ± 0.026			0.545 ± 0.026	
128	0.953 ± 0.045			0.953 ± 0.045	
129	1.691 ± 0.079			1.691 ± 0.079	
130	2.726 ± 0.128		2.328 ± 0.094	2.468 ± 0.076	6.24
131	3.830 ± 0.180		3.496 ± 0.138	3.619 ± 0.109	2.16
132	5.073 ± 0.238	5.470 ± 0.259	5.431 ± 0.205	5.330 ± 0.133	1.69
133	7.182 ± 0.373	7.213 ± 0.337	7.153 ± 0.278	7.178 ± 0.186	0.02
134	6.844 ± 0.335	7.827 ± 0.366	8.123 ± 0.278	7.659 ± 0.185	8.89
135	7.550 ± 0.393	7.496 ± 0.349	8.112 ± 0.444	7.672 ± 0.225	1.34
136	7.272 ± 0.451	6.630 ± 0.315	7.200 ± 0.266	7.015 ± 0.185	2.30
137	6.874 ± 0.419	6.908 ± 0.322	7.537 ± 0.389	7.089 ± 0.214	1.91
138	6.058 ± 0.285	6.053 ± 0.285	5.753 ± 0.301	5.962 ± 0.167	0.70
139	5.680 ± 0.273	5.659 ± 0.270		5.669 ± 0.192	0.00
140	4.785 ± 0.435	5.374 ± 0.262	4.465 ± 0.326	4.975 ± 0.185	4.96
141	5.103 ± 0.464	5.341 ± 0.257	5.200 ± 0.264	5.249 ± 0.171	0.26
142	4.586 ± 0.463	4.310 ± 0.216	3.741 ± 0.146	3.962 ± 0.117	6.71
143	4.049 ± 0.328	4.330 ± 0.211	4.165 ± 0.155	4.201 ± 0.117	0.64
144	4.019 ± 0.326	3.416 ± 0.170		3.546 ± 0.151	2.69
145	3.243 ± 0.230	2.940 ± 0.149		3.029 ± 0.125	1.22
146	2.636 ± 0.137			2.636 ± 0.137	
147	2.248 ± 0.205			2.248 ± 0.205	
148	1.641 ± 0.149			1.641 ± 0.149	
149	1.174 ± 0.106			1.174 ± 0.106	
150	0.877 ± 0.107			0.877 ± 0.107	

experiments are consistent with each other, even for the masses 134 and 142. Obviously, by averaging the three measurements, we were able to reduce the final uncertainties, which are below 5.2% in the $A = [126–146]$ mass range; about 9% for masses 147, 148, and 149; and about 12% for mass 150.

IV. DISCUSSION

The mean data values deduced from our three measurements are also compared with data from JEFF-3.1.1 evaluated nuclear data library in Fig. 6. An overall good agreement can be observed between our data and JEFF-3.1.1 library as shown on the bottom part of the figure, where the relative differences ($\Delta = (J - E)/E$, where J and E stand for JEFF-3.1.1 and experimental data, respectively) are displayed. Only few masses ($A = 127–130, 134, 142$) are not within the Lohengrin experimental uncertainties. The total uncertainties (statistical and systematic) of the present data are much smaller than the uncertainties shown by JEFF-3.1.1. Nevertheless, we have to keep in mind that mass yields are not directly given in the nuclear data library: Only isotopic yields are mentioned. It means that mass yields must be calculated by summing the yields of the isotopic contribution and their uncertainties are deduced from a quadratic sum of the isotopic yield uncertainties, leading to an overestimation of the uncertainties.

The present data on fission fragment yield distribution from ^{239}Pu(n_{th}, f) reaction exhibit several striking features as discussed below.

A. Special case of the mass 134

The independent mass yield for $A = 134$ roughly corresponds to the ^{134}Xe cumulated fission yield. It is due to the fact that the 134 and 135 mass chains contain a negligible number of delayed neutron precursors. Since xenon from ^{239}Pu(n_{th}, f) reaction is released in irradiated MOX fuel, its accurate production information is very important for the fuel burn-up evaluation and therefore our data provide key input for nuclear energy applications. Several striking differences in comparison to nuclear data libraries JEF-2.2 and JEFF-3.1.1 can be observed, in particular for the ^{134}Xe cumulated yield where a dip of around 10% is seen (see Fig. 7). In the past, various measurements [27] have been performed for the independent mass yield of $A = 134$ from thermal neutron-induced fission of ^{239}Pu as shown in the Fig. 7. Out of these measurements for $A = 134$, the first one [28] shows the smallest yield (5.37 ± 0.27)%. The data library JEFF-3.1.1 considers all these measurements, including the first one with the smallest error (highest weight). A ^{134}Xe cumulated yield of (6.87 ± 0.36)% was deduced as shown by the lower hatched region (green color). For the JEF-2.2, the two extreme measurements were excluded, yielding a value

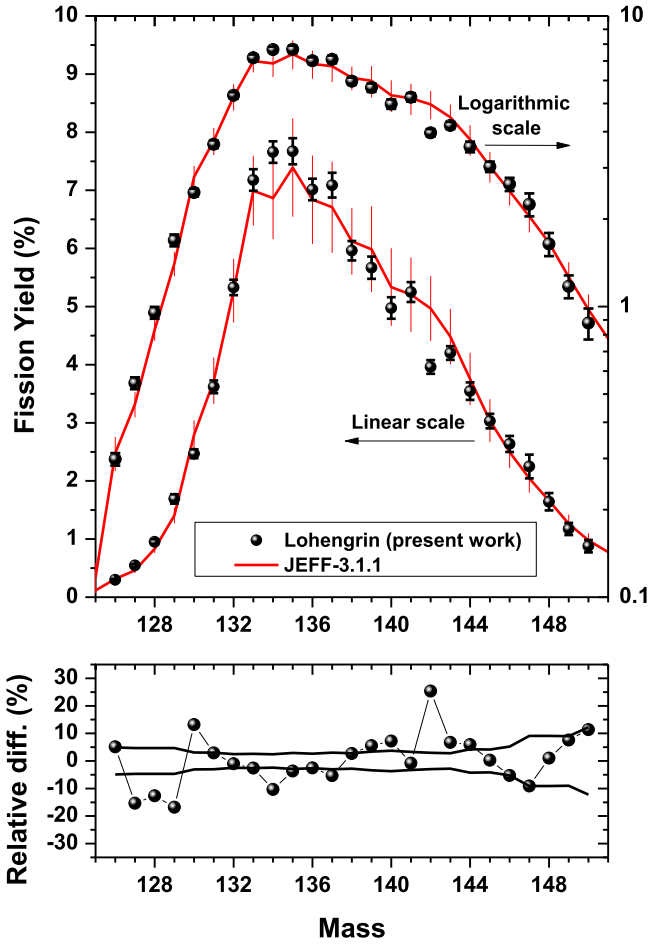

FIG. 6. Relative mass yields obtained by averaging our three Lohengrin experimental campaigns (top, black circles) compared with the JEFF-3.1.1 nuclear data library (top, red line). The left (right) axis gives yield using a linear (logarithmic) scale. The relative differences (JEFF-3.1.1/Lohengrin-1) are also shown (bottom, black circles) with the Lohengrin uncertainties (bottom, black lines).

of (7.56 ± 0.14)% as shown by the upper hatched region (blue color). In the present measurement, we found for the mass yield of $A = 134$ (7.659 ± 0.185)% (red open square), which is fairly consistent with the JEF-2.2 library. The present Lohengrin data rule out any pronounced shell structure at $A = 134$, which otherwise would have been anticipated to explain the 10% dip in the relative mass yield as shown by the revised data library JEFF-3.1.1.

It is worth mentioning here that in the frame of surveillance programs in French pressurized water reactors, a large database has been obtained on fission gas release from punctured rods, in particular for the ^{134}Xe. From a comparison between experimental data of puncturing rods and neutronic calculations, it has been shown [29] that the ^{134}Xe cumulated fission yield given in JEF-2.2 provides consistent results, which gives confidence in the value obtained in the present work.

B. Special case of mass 136

Present data do not exhibit any significant dip around $A = 136$, which is in contrast to heavy-ion fission from ^{208}Pb(^{18}O, f) and ^{238}U(^{18}O, f) reactions [10–12], where significant dips around $A = 124$ and 136 are observed. The observed dips in the heavy-ion mass-yield distribution have been interpreted due to inhibition of spherical shapes of closed-shell ($Z = 50$ and $N = 82$) fragment nuclei at the scission point [12]. It has to be noted here that those heavy-ion data are of large excitation energies (~35 to 50 MeV) of the fissioning nuclei, and fission mass yields are determined from γ-ray yields. Shell effects are more prevalent at lower excitation energies; therefore, the dip at $A = 136$ should have been enhanced in thermal neutron-induced fission. There are few measurements available in literature having mass resolution of the order of one amu. Earlier data from thermal neutron-induced fission of other actinides also do not show a significant reduction in the yield of $A = 136$. This discrepancy might be due to different coordinates on the N/Z chart of $A = 136$ nuclides produced in thermal neutron-induced and heavy-ion fission reactions. The another possibility is underestimated mass yield of $A = 136$ in the heavy-ion fusion-fission reactions because of reduced γ yields from ^{136m}Xe in the prompt gate. Further investigations are required in order to clearly understand the yield discrepancy around $A = 136$ in thermal neutron-induced and heavy-ion fission reactions.

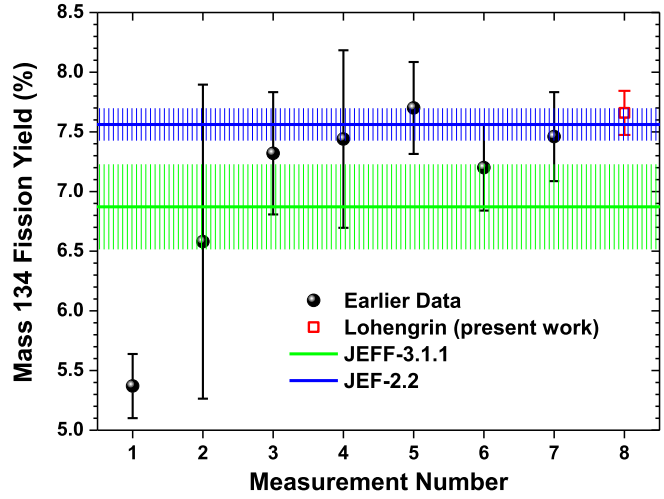

FIG. 7. Relative mass yield for $A = 134$ from thermal neutron-induced fission of ^{239}Pu. Black solid circles correspond to previous measurements [27] on which the JEF-2.2 and JEFF-3.1.1 evaluations reside (see text). The red open square corresponds to the Lohengrin data (present work). The green and blue hatched regions represent the ^{134}Xe cumulated fission yield from JEFF-3.1.1 and JEF-2.2, respectively.

C. Special case of mass 142

As already said in the previous section, strong discrepancies between our three experimental campaigns can be observed for the yield of the mass $A = 142$ (see Table II). This mass is contaminated by the presence of a nanosecond isomer coming from the ^{142}Cs isomeric state, with a half-life of (11 ± 3) ns [30]. Then, the ionic charge distributions are characterized by the presence of a component in the high ionic charge region, similar to the one plotted in Fig. 3. This effect has been also

observed by Beyaev [31] for the mass $A = 142$, but in the case of the ^{241}Pu$(n_{\rm th}, f)$ reaction. Consequently, a correlation between the kinetic energy E_k and the ionic charge q exists and the assumption used for the analysis of the experiments 1 and 2 is no longer valid. In addition, when only one scan across ionic charges and one scan across kinetic energies are performed (as for experiments 1 and 2), the deduced mass yield will be strongly dependent on the ionic charge chosen for performing the kinetic energy scan. For experiment 3, three scans across kinetic energies were carried out at $q = 22$, 25, and 28, leading to a more reliable and accurate mass yield determination. This discussion helps us to understand why mass yields from experiments 1 and 2 are consistent with each other (within one standard deviation) but not consistent with the value obtained from experiment 3. Nevertheless, in the present work, as explained in the previous section, we have decided to keep information from the three experiments. The weighted average yield (3.962 ± 0.117) is close to the value from experiment 3 (due to its reduced uncertainty and therefore its highest weight), which seems quite reasonable.

D. Odd-even staggering

Mass-yield data measured in the present work also exhibit odd-even staggering effects, especially in the mass range between $A = 134$ and 144, as shown in the inset of Fig. 5. In this region, the relative yield of the odd-mass nuclei, viz., $A = 135$, 137, 139, 141, and 143 is either equal or slightly higher than the neighboring even-mass nuclei. This effect is more pronounced in our data than in the JEFF-3.1.1 libraries. For example, the mass yield of $A = 142$ from this work is noticeably lower (3.962 ± 0.117)% than those shown by both data libraries, which are in mutual agreement with each other for this mass value: (4.96 ± 0.55)% and (5.03 ± 0.56)% from JEFF-3.1.1 and JEF-2.2, respectively. This odd-even effect seems to be correlated with the strong odd-even effect observed in the nuclear charge yield between $Z = 52$ and 56 [14]. Indeed, for a given mass, the most probable charge Z_p is rather well estimated by $Z_p = Z_{UCD} - \Delta_p$, where Z_{UCD} is the nuclear charge deduced from the unchanged charge distribution model and Δ_p the polarization charge. Assuming a constant polarization charge ($\Delta_p = +0.5$ [15]), we obtain $Z_p \sim 52$ and $Z_p \sim 56$, for the masses $A = 132$ and 144, respectively, which is precisely the mass range where the odd-even staggering is observed. Obviously, we must keep in mind that this effect is strongly affected by the emission of prompt neutrons.

E. Comparison with GEF and FIFRELIN codes

Our experimental data are also compared with calculations performed with the GEF [32] and FIFRELIN [33,34] codes. Both codes are briefly described.

(1) The GEF Monte Carlo code, developed recently by Schmidt *et al.* [32], first calculates the preneutron mass yield (before prompt neutron emission) using the concept of fission modes developed by Brosa *et al.* [35]. These fission modes correspond to the valleys in the potential energy surface which can be followed by the fissioning nucleus. The depth and the width of each mode are determined in order to deduce fission-fragment properties (yield, deformation of the nascent fission fragments at the scission point, kinetic energy, etc.). Then, the total excitation energy available at scission is shared between the two fragments and a statistical treatment is applied for simulating the emission of prompt neutrons and prompt gamma particles. As said in Ref. [32] (p. 107), "fission observables can be calculated with a precision that complies with the needs for applications in nuclear technology without specific adjustments to measured data of individual systems" (p. 107). Among these fission observables, postneutron mass yields (after prompt neutron emission) can be calculated and compared with our experimental data. All the details related to the GEF code can be found in Ref. [32].

(2) The FIFRELIN Monte Carlo code, developed at CEA-Cadarache, is based on a different philosophy. To start a FIFRELIN calculation, preneutron yield and kinetic energy are needed for each mass. Then, the total available excitation energy at scission is determined and shared between both fission fragments using an empirical temperature ratio law. The deexcitation of the fission fragments is simulated from the Hauser-Feschbach theory [36] by following the Becvar procedure [37] extended to n/γ coupled emission [38]. In this way, postneutron mass yields can be deduced as well as various other fission observables. As explained in detail in Refs. [33,34], five free parameters are involved in the calculation, which are adjusted in order to reproduce the total average prompt neutron multiplicity ($\langle \nu_P \rangle = 2.87$ in the case of ^{239}Pu$(n_{\rm th}, f)$ reaction). Two independent FIFRELIN calculations were performed. The first one (called hereafter FIFRELIN/Dematté) uses the preneutron data from the Dematté experiment [39,40]. The second FIFRELIN calculation (called hereafter FIFRELIN/GEF) uses the preneutron data provided by the GEF code. In this way, the impact of the preneutron data on the calculation of the postneutron fission yields can be investigated.

Figure 8 shows the comparison between our experimental data and the three calculations described above. The bottom part of the figure corresponds to the relative differences ($\Delta = (C - E)/E$, where C and E stand for calculated and experimental data, respectively). Looking at the GEF calculation (left part of the Fig. 8), an overall very good agreement can be observed. Only four masses ($A = 126$, 127, 136, 142) disagree with Lohengrin data by more than 15%. The FIFRELIN/Dematté calculation (red line in the right part of the Fig. 8) shows also a nice agreement with Lohengrin data, especially in the mass range $A = [134–150]$ (with the exception of the mass 142). Nevertheless, strong discrepancies can be noticed below $A = 128$. It is interesting to note that the FIFRELIN/Dematté calculation tends to improve the agreement with Lohengrin data compared to the FIFRELIN/GEF calculation (green line in the right part of the Fig. 8). Three different mass regions can be distinguished:

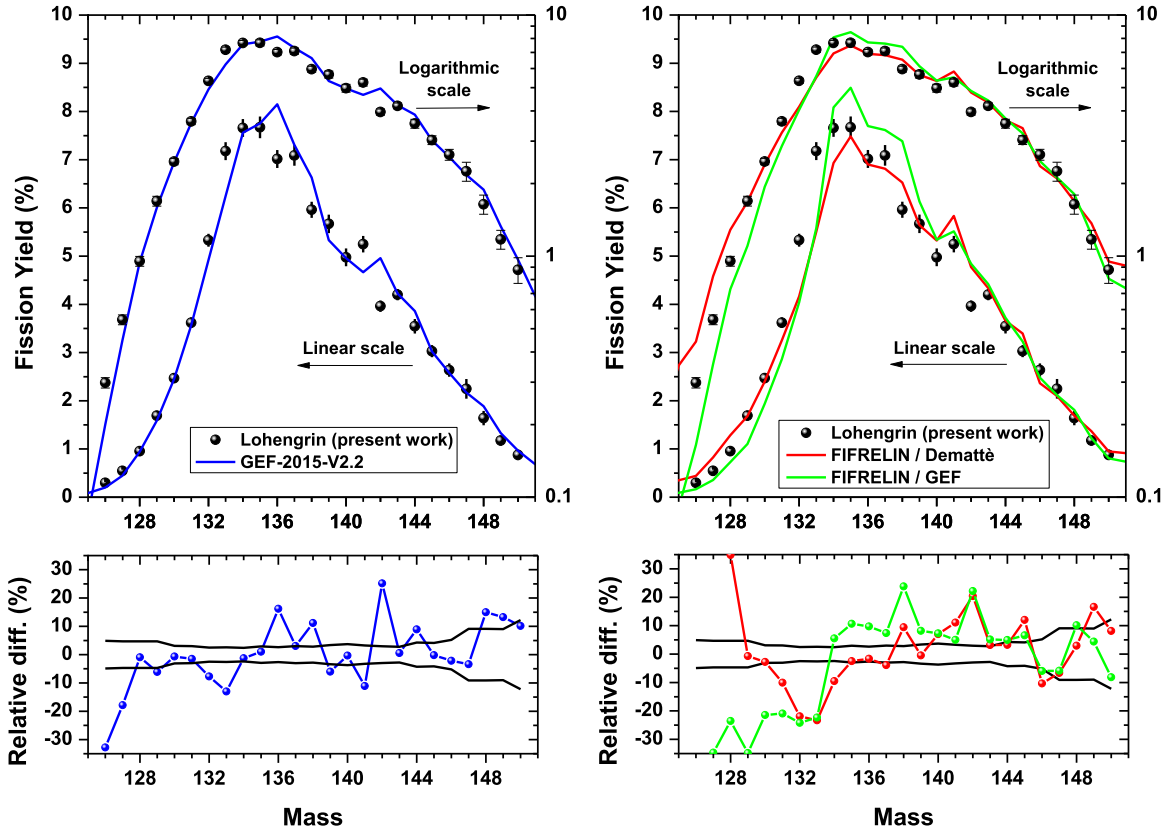

FIG. 8. Measured heavy mass yields (black circles) compared with the (i) GEF calculation (left part, blue line), (ii) FIFRELIN calculations using Dematté preneutron mass yield (right part, red line) and (iii) FIFRELIN calculations using GEF preneutron mass yield (right part, green line). The left (right) axis gives yield using a linear (logarithmic) scale. Relative differences between calculated and experimental data ($C/E - 1$) are shown on the bottom part of the figure with the experimental uncertainties (black lines).

(1) Below $A = 132$, yields from FIFRELIN/Dematté are systematically higher than the one from FIFRELIN/GEF calculation.
(2) Between $A = 133$ and 140, the reverse situation to that of below $A = 132$ occurs.
(3) In the mass range $A = [141–148]$, both FIFRELIN calculations give similar yields.

These differences are correlated with the preneutron mass yields, used as input data in our two FIFRELIN calculations. Indeed, as shown in the Fig. 9, below the mass 132 where the standard I fission mode is predominant, the preneutron yields from the Dematté experiment are higher than the preneutron yields predicted by GEF, suggesting that the standard I fission mode characteristics (width and/or weight) are different. Similarly, above the mass 151, the Dematté preneutron yields are higher than the GEF prediction, underlying the different weight of the superasymmetric fission mode. In the mass range between $A = 133$ and 150, the Dematté preneutron yields are either lower or similar to the GEF preneutron yields, showing the impact of the standard II fission mode characteristics.

Lastly, we have to mention that discrepancies observed between GEF and FIFRELIN codes are also due to the different procedures used for simulating the prompt neutron emission which has obviously an impact on the calculation of the postneutron mass yields. This aspect is illustrated in Fig. 10, where the calculated average prompt neutron multiplicities as a function of mass (the so-called saw-tooth curves), including also the data from Wahl's evaluation [23], are plotted. In our

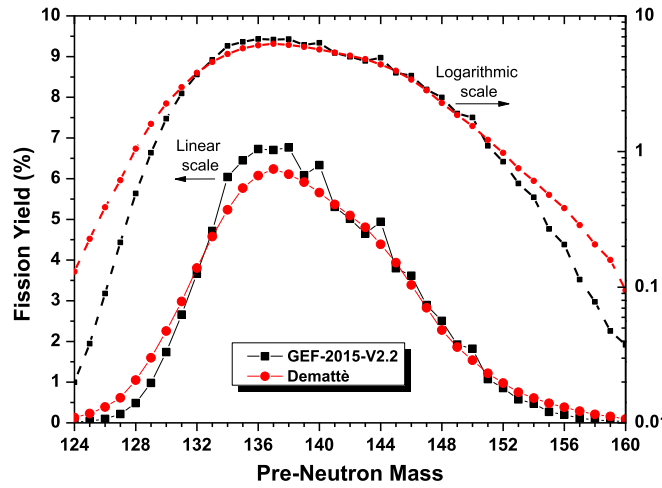

FIG. 9. Preneutron mass yields used as input data for our two FIFRELIN calculations. Black points correspond to the preneutron yields predicted by the GEF code, while red points correspond to the Dematté experimental data [39,40]. The left (right) axis gives yield using a linear (logarithmic) scale.

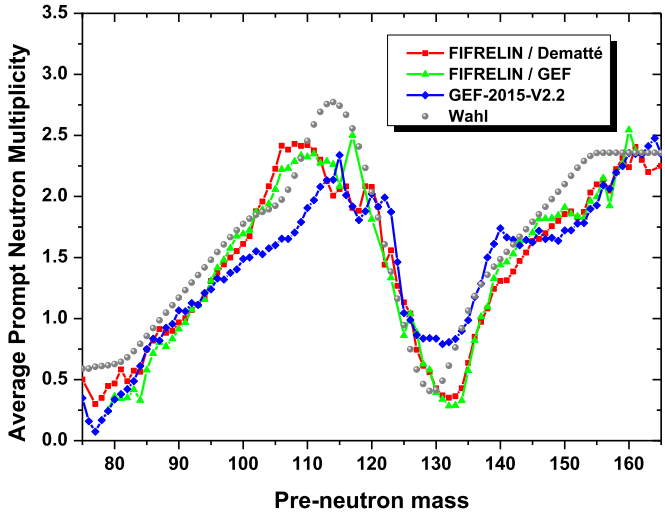

FIG. 10. Average prompt neutron multiplicity as a function of the preneutron mass obtained from the three following calculations: FIFRELIN/Dematté (red solid squares), FIFRELIN/GEF (green solid triangles), and GEF (blue solid diamonds). Wahl's evaluation [23] is also shown (gray solid circles).

region of interest, i.e., the heavy-mass region, these saw-tooth curves show significant differences, especially between mass 125 and mass 135.

V. SUMMARY

The fission fragment mass distribution in ^{239}Pu$(n_{\rm th}, f)$ reaction is obtained in the range of $A = 126$ to 150 using the Lohengrin recoil-mass spectrometer located at the Institut Laue-Langevin in Grenoble (France). Three independent experiments were performed, allowing us to significantly reduce the total uncertainties. An overall good agreement with JEFF-3.1.1 fission yield evaluation, except for the mass 134, which is important for nuclear applications, is observed. Indeed, unlike the evaluated data library JEFF-3.1.1, which shows a 10% dip at $A = 134$, the present data show a smooth behavior consistent with the data library JEF-2.2. The present data do not exhibit any significant dip around $A = 136$, in contrast to heavy-ion fission from ^{208}Pb(^{18}O, f) and ^{238}U(^{18}O, f) reactions [10–12]. The present results are important from the point of extensive efforts being made in reducing the uncertainties and can be useful for the next release of the fission yield evaluations as well as for validating nuclear fission models implemented in recent Monte Carlo codes (such as GEF or FIFRELIN).

ACKNOWLEDGMENTS

We are indebted to the Lohengrin operating team for the optimum conditions during the measurements. We acknowledge the financial support received from the NEEDS partnership, an interdisciplinary research effort on Nuclear Energy, Environment, Waste and Society between French organizations (CNRS, Universities, CEA, IRSN, EDF, AREVA, ANDRA and BRGM). The first two authors are thankful to Dr. R. K. Choudhury for many useful discussions.

[1] J. Moreau and K. Heyde, *The Nuclear Fission Process*, edited by C. Wagemans (CRC Press, Boca Raton, FL, 1991).
[2] B. D. Wilkins, E. P. Steinberg, and R. R. Chasman, Phys. Rev. C **14**, 1832 (1976).
[3] P. Möller, D. G. Madland, A. J. Sierk, and A. Iwamoto, Nature (London) **409**, 785 (2001).
[4] H. Goutte, J. F. Berger, P. Casoli, and D. Gogny, Phys. Rev. C **71**, 024316 (2005).
[5] D. Regnier, N. Dubray, N. Schunck, and M. Verrière, Phys. Rev. C **93**, 054611 (2016).
[6] M. Kellett, JEF-2.2 Nuclear Data Library (OECD, Paris, 2000).
[7] M. Kellett, JEFF Report 20, NEA NØ6287 (OECD, Paris, 2009).
[8] M. B. Chadwick, P. Oblozinsky, M. Herman, N. M. Greene, R. D. McKnight, D. L. Smith, P. G. Young, R. E. MacFarlane, G. M. Hale, S. C. Frankle *et al.*, Nucl. Data Sheets **107**, 2931 (2006).
[9] K. Shibata, O. Iwamoto, T. Nakagawa, N. Iwamoto, A. Ichihara, S. Kunieda, S. Chiba, K. Furutaka, N. Otuka, and T. Oshasawa, J. Nucl. Sci. Technol. **48**, 1 (2011).
[10] A. Bogachev, L. Krupa, O. Dorvaux, M. Itkis, M. G. Porquet, A. Astier, D. Curien, I. Deloncle, G. Duchene, B. J. P. Gall *et al.*, Eur. Phys. J. A **34**, 23 (2007).
[11] P. Banerjee, S. Ganguly, M. K. Pradhan, M. M. Shaikh, H. P. Sharma, S. Chakraborty, R. Palit, R. G. Pillay, V. Nanal, S. Saha *et al.*, Phys. Rev. C **92**, 024318 (2015).
[12] L. S. Danu, D. C. Biswas, A. Saxena, A. Shrivastava, A. Chatterjee, B. K. Nayak, R. G. Thomas, R. K. Choudhury, R. Palit, I. Mazumdar *et al.*, Phys. Rev. C **81**, 014311 (2010).
[13] O. Serot, C. Amouroux, A. Bidaud, N. Capellan, S. Chabod, A. Ebran, H. Faust, G. Kessedjian, U. Köster, A. Letourneau *et al.*, Nucl. Data Sheets **119**, 320 (2014).
[14] H. G. Börner and F. Gönnenwein, *The Neutron, a Tool and an Object in Nuclear and Particle Physics* (World Scientific, Singapore, 2012).
[15] A. Bail, O. Serot, L. Mathieu, O. Litaize, T. Materna, U. Köster, H. Faust, A. Letourneau, and S. Panebianco, Phys. Rev. C **84**, 034605 (2011).
[16] Y. K. Gupta, D. C. Biswas, U. Köster, O. Serot, A. Chatterjee, and S. Kailas, in *Proceedings of the Department of Atomic Energy Symposium on Nucl. Phys.*, edited by S. R. Jain, P. Shukla, A. Chatterjee, and V. M. Datar (Department of Atomic Eneregy, Mumbai, 2012), Vol. 57, p. 402, www.sympnp.org/proceedings.
[17] A. Chebboubi, G. Kessedjian, S. Julien-Laferrière, C. Sage, O. Meplan, H. Faust, U. Köster, A. Blanc, P. Mutti, O. Serot *et al.*, JEF/DOC 1717 (OECD/NEA, Paris, 2015).
[18] U. Köster, H. Faust, T. Materna, and L. Mathieu, Nucl. Instrum. Methods A **613**, 363 (2010).
[19] P. Armbruster, M. Asghar, J. Bocquet, R. Decker, H. Ewald, J. Greif, E. Moll, B. Pfeiffer, H. Schrader, F. Schussler *et al.*, Nucl. Instrum. Methods **139**, 213 (1976).

[20] G. Fioni, H. R. Faust, M. Gross, M. Hesse, P. Armbruster, F. Gönnenwein, and G. Münzenberg, Nucl. Instrum. Methods **332**, 175 (1993).
[21] H. Wohlfarth, W. Lang, H. Dann, H. G. Clerc, K. H. Schmidt, and H. Schrader, Z. Phys. A **287**, 153 (1978).
[22] T. Materna, A. Bail, L. Mathieu, U. Köster, H. Faust, O. Serot, and F. Michel-Sendis, in *AIP Conference Proceedings, Cadarache (France)* (AIP, Melville, New York, 2009), Vol. 1175, p. 367.
[23] A. C. Wahl, At. Data Nucl. Data Tables **39**, 1 (1988).
[24] N. Nica, Nucl. Data Sheets **108**, 1287 (2007).
[25] F. Martin, C. Sage, G. Kessedjian, O. Serot, C. Amouroux, C. O. Bacri, A. Bidaud, A. Billebaud, N. Capellan, S. Chabod *et al.*, Nucl. Data Sheets **119**, 328 (2014).
[26] S. Julien-Laferrière (unpublished).
[27] R. Mills (private communication).
[28] W. H. Fleming and H. G. Thode, Can. J. Chem. **34**, 193 (1956).
[29] F. Lemoine, O. Serot, P. Leconte, and D. Bernard, in *Proceedings of Water Reactor Fuel Performance Meeting, Sendai, Japan, Sept. 14–17, 2014* (IAEA, 2014), p. 100130.
[30] T. Rzaca-Urban, J. Genevey, T. Materna, W. Urban, A. G. Smith, J. A. Pinston, G. S. Simpson, M. P. Sadowski, U. Köster, H. Faust *et al.*, Phys. Rev. C **80**, 064317 (2009).
[31] A. D. Belyaev, Z. S. Bikbova, V. L. Gaishan, T. L. Gurvich, V. I. Kogan, V. P. Pikul, and A. M. Usmandiyarov, Nucl. Instrum. Methods Phys. Res., Sect. B **43**, 5 (1989).
[32] K. H. Schmidt, B. Jurado, C. Amouroux, and C. Schmitt, Nucl. Data Sheets **131**, 107 (2016).
[33] O. Litaize and O. Serot, Phys. Rev. C **82**, 054616 (2010).
[34] O. Litaize, O. Serot, and L. Berge, Eur. Phys. J. A **51**, 177 (2015).
[35] U. Brosa, S. Grossmann, and A. Müller, Phys. Rep. **197**, 167 (1990).
[36] W. Hauser and H. Feshbach, Phys. Rev. **87**, 366 (1952).
[37] F. Becvar, Nucl. Instrum. Methods Phys. Res., Sect. A **417**, 434 (1998).
[38] D. Regnier, O. Litaize, and O. Serot, Comput. Phys. Commun. **201**, 19 (2016).
[39] L. Demattè, C. Wagemans, R. Barthélémy, P. D'hondt, and A. Deruytter, Nucl. Phys. A **617**, 331 (1997).
[40] L. Demattè, Ph.D. thesis, University of Gent, Belgium, 1997 (unpublished).